

Direct state measurements under state-preparation-and-measurement errors

Kieu Quang Tuan,¹ Hung Q. Nguyen,² and Le Bin Ho^{3,4}

¹University of Science, VNUHCM, Ho Chi Minh City, Vietnam

²Nano and Energy Center, VNU University of Science,
Vietnam National University, 120401, Hanoi, Vietnam

³Ho Chi Minh City Institute of Physics, VAST, Ho Chi Minh City, Vietnam

⁴Research Institute of Electrical Communication, Tohoku University, Sendai, 980-8577, Japan*

(Dated: May 27, 2021)

Direct state measurement (DSM) is a tomography method that allows for retrieving quantum states' wave functions directly. However, a shortcoming of current studies on the DSM is that it does not provide access to noisy quantum systems. Here, we attempt to fill the gap by investigating the DSM measurement precision that undergoes the state-preparation-and-measurement (SPAM) errors. We manipulate a quantum controlled measurement framework with various configurations and compare the efficiency between them. Under such SPAM errors, the state to be measured lightly deviates from the true state, and the measurement error in the postselection process results in less accurate in the tomography. Our study could provide a reliable tool for SPAM errors tomography and contribute to understanding and resolving an urgent demand for current quantum technologies.

I. INTRODUCTION

In quantum measurement, a process for retrieving the wave functions of quantum states is known as quantum state tomography (QST) [1]. It plays a crucial role in a wide range of quantum technologies, from randomized benchmarking [2], calibrating quantum operations [3], to experimentally validating quantum computing devices [4].

However, the most severe obstacle against the realizing quantum devices, such as the current version of noisy intermediate-scale quantum (NISQ) computers, is that the noise can result in the superposition and entanglement loss. Typically, the noise can occur by the imperfection over controlling the system [5] or when the system inevitably interacts with its surrounding environment [6]. Such noises appear during the preparation and measurement processes can be referred to as state-preparation-and-measurement (SPAM) errors [7] and thus limit the accuracy of quantum tomography (or quantum measurement in general.) In this work, we model and evaluate the effect of such SPAM errors in a direct state measurement scheme.

Besides the conventional quantum state tomography [8–11] in which particularly challenging for large systems, a direct state measurement (DSM) method was proposed [12, 13] and extensively used. This method is straightforward, versatile, simple, and has been numerously applied in large systems [14–18], mixed quantum states [13, 19, 20], enlarged Hilbert space [21], and non-local entangled states [22]. Further study on the novelty, efficacy, and significance of the DSM had been reported [23]. So far, the statistical error and systematic error have been examined [24–26].

The measurement employed in the DSM follows the von Neumann interaction and requires a postselection

technique [27]. Recently, however, a quantum controlled measurement framework has been proposed [28, 29] and can be used for analyzing systematic errors in the DSM [26]. This framework contains a probe-controlled-system type of the interaction where a qubit probe controls a target system through the evolution [29]

$$\mathbf{U} = \mathbf{U}_0 \otimes |0\rangle\langle 0| + \mathbf{U}_1 \otimes |1\rangle\langle 1|, \quad (1)$$

where $\mathbf{U}_0, \mathbf{U}_1$ are the operators of the target system, and $|0\rangle, |1\rangle$ are two elements of the basis in the control qubit probe. Such an interaction can be realized by using a Fredkin gate, as illustrated in Fig. 1(a). This measurement scheme is operationally equivalent to the von Neumann interaction [26]. Moreover, when combining with the postselection technique, it allows for cyclic transforming the system operators, which results in different configurations [29]. See, for example, configurations C1, C2 in Fig. 1(c, d) below. In some configurations, a scan-free technique [14] can be used directly, which assists in improving the measurement precision.

In this work, we numerically and analytically investigate the measurement efficiency in the DSM that both the pre- and postselected states are under the noises during the preparation and measurement (postselection) processes. These noises can be seen as SPAM errors. We consider two cases of noise: (i) noisy in pure states due to the imperfection, and (ii) noisy in mixed states due to the interaction with the surrounding environment. Previously, Shikano and Hosoya had proposed such a noisy system due to its interaction with the surrounding environment [30].

We employ the quantum controlled measurement framework with different configurations under SPAM errors and compare their efficiencies. We use the mean trace distance obtained from the Monte Carlo simulation to evaluate the measurement precession. Noting that through this paper, we refer to the SPAM errors as “noises” that occur during the state-preparation and postselection processes. Besides, we also use the “sys-

* Electronic address: binho@riec.tohoku.ac.jp

tematic error” and “statistical error” terminologies for the measurement precision. The systematic error is typically caused by the different configurations of the measurement scheme [26], while the statistical error regards the finite number of the repeated measurements.

The rest of this paper is organized as follows. In Sec. II, we define SPAM errors and two configurations of the quantum controlled measurement framework for pure states and then extend to mixed states. The numerical results are presented in Sec. III for both cases of pure and mixed quantum states. In Sec. IV, we analytically investigate the impact of the state-preparation error on the precision in the reconstruction process. Finally, we summarize our work in Sec. V.

II. DIRECT STATE MEASUREMENT WITH QUANTUM CONTROLLED INTERACTION

We first consider the SPAM errors for pure-state quantum systems and then generalize to mixed states. Typically, a direct state measurement framework includes (i) the coupling between a quantum target system and a control qubit probe, (ii) the postselection of the target system onto a final state, (iii) and the measurement on the control qubit probe.

A. State-preparation and state-postselection errors for pure states

Assume that a pure quantum state is spanned in a computational basis $\{|n\rangle\}_0^{d-1}$ of a system d -dimensional space as follows

$$|\psi\rangle = \sum_{n=0}^{d-1} \psi_n |n\rangle, \quad (2)$$

where $\psi_n \equiv \langle n|\psi\rangle$ is a complex amplitude and satisfies $\sum_n |\psi_n|^2 = 1$. We model a noise in the state-preparation system due to the “imperfection” during the preparation process [5]. See an example in App. A. In general, we assume that under such an imperfection, the original quantum state transforms into

$$|\psi\rangle \rightarrow |\psi'\rangle = \frac{1}{\mathcal{N}} \sum_n (\psi_n + \delta_n) |n\rangle, \quad (3)$$

where \mathcal{N} is a normalization constant, and δ_n is a complex random perturbation, i.e., $\delta_n = x_1 + ix_2$, where x_1, x_2 are random numbers and obey the normal distribution with mean zero, such that $f(x) = \frac{1}{\sigma\sqrt{2\pi}} \exp[-\frac{1}{2}(\frac{x}{\sigma})^2]$. Here, σ is the standard derivation, which stands for the noise parameter. Under such perturbation, $|\psi'\rangle$ can be seen as a “probability distribution” of state $|\psi\rangle$. Here, we consider this simple case to evaluate the efficiency of the proposed protocol for pure states.

A spin-based visualization for $|\psi\rangle$ and an ensemble of $|\psi'\rangle$'s is illustrated in Fig. 1(b). Therein, the red-filled circle is the true state $|\psi\rangle$, and the open circles are the

statistical distribution of $|\psi'\rangle$'s. We emphasize that the noise parameter is unknown, therein it lightly deviates the quantum state $|\psi'\rangle$ from the original quantum state $|\psi\rangle$. Therefore, to evaluate the measurement efficiency under the noise, we need to compare the reconstructed state with the true state. This method has widely used in the QST under noise [31, 32].

For the noisy state-postselection, in the same spirit as the noisy state-preparation, we assume that the postselected state $|\phi\rangle$ contains a small noise, and thus it becomes

$$|\phi'\rangle \equiv |\mathbf{c}'_0\rangle = \frac{1}{\mathcal{M}} \sum_m (1 + \kappa_m) |m\rangle = \sum_m \mathbf{c}_m |m\rangle, \quad (4)$$

where \mathcal{M} is the normalization factor, $\mathbf{c}_m = \frac{1+\kappa_m}{\mathcal{M}}$, and κ_m is a random number. We illustrate the noisy state-postselection in Fig. 1(b). If a detector is perfect, it will detect exactly the state (or position) at each $|m\rangle$. Inversely, if there is imperfection, the detector will detect a biased state, i.e., $|m\rangle + \kappa_m |m\rangle$. Without loss of generality, we can assume κ_m is real and follows the normal distribution because the complex part of the postselected state can be absorbed into the phase (see Eq. (13).) Together, the noisy state-preparation and state-postselection form SPAM errors.

This simple case of the SPAM errors is used for evaluating the performance of the measured protocol for pure states. Besides, such imperfections are widespread in the current version of the NISQ computers [5]. It is thus helpful to study such noise in quantum tomography, an essential aspect of the NISQ.

Furthermore, similar to Ref. [30], here we draw our attention to the role of the SPAM errors in the target system, which affects the tomography process itself. We thus, restrict ourselves to the case where the control qubit is pure and perfectly prepared. In practical realization, the qubit probe can be prepared such that it is error-free. For example, in photonics systems, the control qubit probe is the photon polarization mode, which can be realized using polarizers (optical filters) [14, 29]. Hence, the noise in such a qubit probe can be eliminated.

B. Quantum controlled measurements for pure states

We first consider Configuration 1 (or C1 for short), described by an interaction scheme between a target system and a control qubit probe. The measurement scheme is schematically shown in Fig. 1(c). The initial state of the target system is $|\psi'\rangle$, while the control qubit is initially prepared in the state $|\xi\rangle$, i.e., $|\xi\rangle \equiv |+\rangle = (|0\rangle + |1\rangle)/\sqrt{2}$. The initial joint state becomes $|\Psi\rangle = \sum_n \psi'_n |n\rangle \otimes |+\rangle$, where $\psi'_n = (\psi_n + \delta_n)/\mathcal{N}$. The interaction between the target system and the control qubit probe is given by

$$U_n = (\mathbf{I}_s - |n\rangle\langle n|) \otimes |0\rangle\langle 0| + |n\rangle\langle n| \otimes |1\rangle\langle 1|, \quad (5)$$

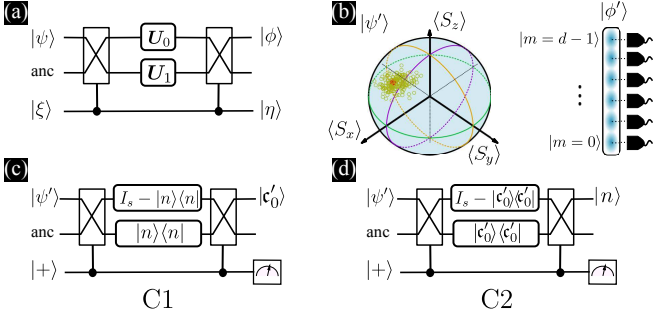


FIG. 1. (a) A quantum controlled measurement scheme for the direct state measurements: $|\psi\rangle$ and $|\phi\rangle$ are pre- and post-selected states in the target system which will become $|\psi'\rangle$ and $|\phi'\rangle$ under the SPAM errors; $|\xi\rangle$ and $|\eta\rangle$ are the initial and final states in the control qubit probe. The action of U_0 or U_1 onto the target state $|\psi\rangle$ is controlled by the control qubit probe via a Fredkin gate with an ancillary (anc) system. (b) A visualization of a noisy state-preparation $|\psi'\rangle$. The red-filled circle is the original state, and the open circles stand for the noisy states, which lightly deviate from the original one. Here $\langle S_i \rangle$, $i = \{x, y, z\}$ are the expectation values of the total spin operators. The noisy state-postselection $|\phi'\rangle$ is also illustrated. (c, d) Two configurations of the quantum controlled measurement scheme. In (c), when the control qubit probe is in state $|0\rangle$, the operator $U_0 = \mathbf{I}_s - |n\rangle\langle n|$ will operate on the target system; while that will be $U_1 = |n\rangle\langle n|$ when the state is $|1\rangle$ (the target state will be swapped). The target system afterward is postselected onto the final state $|\xi'_0\rangle$. The role of $|n\rangle$ and $|\xi'_0\rangle$ can be interchanged to form the configuration C2 in (d).

where \mathbf{I}_s is the identity matrix in the target system. The action of Eq. (5) on the probe state $|\xi\rangle$ is operationally equivalent to a von Neumann measurement given by a strong interaction $U = \exp(-i\frac{\pi}{2}|n\rangle\langle n| \otimes \sigma_y)$ acts on the control qubit prepared in $|0\rangle$ [26, 29]. Particularly, we have $U(\mathbf{I}_s \otimes |0\rangle) = (\mathbf{I}_s - |n\rangle\langle n|) \otimes |0\rangle + |n\rangle\langle n| \otimes |1\rangle$. We thus can choose $U_0 = \mathbf{I}_s - |n\rangle\langle n|$ and $U_1 = |n\rangle\langle n|$ as can be seen in Eq. (5).

After the interaction, we postselect the target system onto the conjugate basis $|\xi'_0\rangle$ as given in Eq. (4). Then, the final control qubit state is given by (see App. B)

$$|\eta\rangle = \frac{1}{\sqrt{2}} \left[(\Gamma - \mathbf{c}_n \psi'_n) |0\rangle + \mathbf{c}_n \psi'_n |1\rangle \right], \quad (6)$$

where we have set $\Gamma = \sum_m \mathbf{c}_m \psi'_m$, which can be chosen to be real [33].

Finally, we measure the control qubit probe in the Pauli basis $\{|j\rangle\}$, where $|j\rangle \in \{|0\rangle, |1\rangle, |+\rangle, |-\rangle, |L\rangle, |R\rangle\}$, $|\pm\rangle = \frac{1}{\sqrt{2}}(|0\rangle \pm |1\rangle)$, $|L\rangle = \frac{1}{\sqrt{2}}(|0\rangle + i|1\rangle)$, $|R\rangle = \frac{1}{\sqrt{2}}(|0\rangle - i|1\rangle)$. The corresponding probability is $P_j = \langle \eta | j \rangle \langle j | \eta \rangle = |\langle j | \eta \rangle|^2$, where the subscript j takes 0, 1, +, -, L, and R corresponding to the elements in the Pauli basis. Then, the real and imaginary parts of the amplitude ψ'_n are reproduced as

$$\text{Re}\psi'_n = \frac{P_+ - P_- + 2P_1}{\mathbf{c}_n \Gamma}, \quad \text{Im}\psi'_n = \frac{P_L - P_R}{\mathbf{c}_n \Gamma}. \quad (7)$$

In this scheme, it is worth noting that after postselecting the target system onto $|\xi'_0\rangle$, we discard all these other results and then repeat the measurement for all $\{n\}$.

Next, we describe Configuration 2 (or C2 for short). In this case, we interchange the role of $|n\rangle$ and $|\xi'_0\rangle$ as shown in Fig. 1(d). The interaction is given by

$$U = (\mathbf{I}_s - |\xi'_0\rangle\langle \xi'_0|) \otimes |0\rangle\langle 0| + |\xi'_0\rangle\langle \xi'_0| \otimes |1\rangle\langle 1|. \quad (8)$$

The random noise κ_m that appear in $|\xi'_0\rangle$ is unknown. Therefore, in practice, this interaction can be done by applying the state $|\xi_0\rangle$ and $|\xi_0\rangle^\perp = \mathbf{I}_s - |\xi_0\rangle\langle \xi_0|$ onto the target system while κ_m is “self-rising” during the measurement process.

After the interaction, the target system is postselected onto the basis $|n\rangle$ while the remaining state of the control qubit probe is given by

$$|\eta\rangle = \frac{1}{\sqrt{2}} \left[(\psi'_n - \mathbf{c}_n \Gamma) |0\rangle + \mathbf{c}_n \Gamma |1\rangle \right]. \quad (9)$$

Measuring the control qubit probe in the Pauli basis as above, we obtain

$$\text{Re}\psi'_n = \frac{P_+ - P_- + 2P_1}{\mathbf{c}_n \Gamma}, \quad \text{Im}\psi'_n = \frac{P_L - P_R}{\mathbf{c}_n \Gamma}. \quad (10)$$

(See App. B for detailed calculation.)

We emphasize that different from C1, here, we keep all the postselected state $\{|n\rangle\}$. This technique is known as “scan-free,” and can be employed by using an array detector [14, 29].

C. Quantum controlled measurements for mixed states

We now consider the general case of SPAM errors for mixed states. Assume the initial target system state is prepared in ρ_0 . It will transform into ρ'_0 by passing through the noise channel \mathcal{E} , such that [34]

$$\rho'_0 \equiv \mathcal{E}(\rho_0) = \sum_k E_k \rho_0 E_k^\dagger, \quad (11)$$

where E_k is an operation element satisfying the completeness relation $\sum_k E_k^\dagger E_k = \mathbf{I}$. Noting that this noise model can be applied for any noise.

Then, the state of the joint target-control system is

$$\Lambda = \rho'_0 \otimes |+\rangle\langle +|, \quad (12)$$

where ρ'_0 can be expressed as $\sum_{n,m=0}^{d-1} \rho'_{nm} |n\rangle\langle m|$, which is the state to be reconstructed after passing through the noisy channel, and $|+\rangle$ is the initial state of the control qubit probe. Here, we will reconstruct the components ρ'_{nm} .

For C1, the target-control interaction is the same as pure-state case, i.e., $U_n = (\mathbf{I}_s - |n\rangle\langle n|) \otimes |0\rangle\langle 0| + |n\rangle\langle n| \otimes$

$|1\rangle\langle 1|$, and the postselected state under the noise is given by

$$|\mathbf{c}'_k\rangle\langle\mathbf{c}'_k| = \sum_{n,m} e^{i2\pi(m-n)k/d} \mathbf{c}_m \mathbf{c}_n |m\rangle\langle n|, \quad (13)$$

where $\mathbf{c}_m = \frac{1+\kappa_m}{\mathcal{M}}$. Using Fourier transformation, we obtain the reconstructed state as

$$\rho'_{nm} \propto \frac{1}{\mathbf{c}_n \mathbf{c}_m} \left[d\delta_{n,m} \Lambda''_{11}(n,k) + \sum_{k=0}^{d-1} e^{\frac{i2\pi(n-m)k}{d}} \Lambda''_{10}(n,k) \right], \quad (14)$$

where $\Lambda''_{ij}(n,k)$ is a component in the final probe state. (See App. C for detailed calculation.)

For C2, the interaction is $U_k = (\mathbf{I}_s - |\mathbf{c}'_k\rangle\langle\mathbf{c}'_k|) \otimes |0\rangle\langle 0| + |\mathbf{c}'_k\rangle\langle\mathbf{c}'_k| \otimes |1\rangle\langle 1|$, and the postselected state is $|n\rangle\langle n|$. The reconstructed state is given by

$$\rho'_{nm} \propto \frac{1}{\mathbf{c}_n \mathbf{c}_m} \left[\sum_{k=0}^{d-1} e^{\frac{i2\pi k(n-m)}{d}} \left(\Lambda''_{01}(n,k) + \Lambda''_{11}(n,k) \right) \right]. \quad (15)$$

(See App. C for detailed calculation.) The reconstructed state ρ' whose elements are ρ'_{nm} is not a physical state. The normalized state of ρ' is denoted as $\tilde{\rho}$ and given by $\tilde{\rho} = \rho'^{\dagger} \rho' / \text{Tr}(\rho'^{\dagger} \rho')$, which is a normalized Hermitian matrix, and thus it is a physical state [1].

We emphasize that in the mixed-state case, both C1 and C2 can implement the scan-free technique because we can keep all postselected states $\{|\mathbf{c}'_k\rangle\langle\mathbf{c}'_k|\}$ in C1 and all postselected states $\{|n\rangle\langle n|\}$ in C2 without discarding them.

III. NUMERICAL RESULTS

A. Numerical results for pure states

We employ a simulation scheme using the cumulative distribution function (cdf) [21, 35], that built in to *qtix* [36]. To evaluate the accuracy of the reconstruction, we use the trace distance as a figure of merit, defined by

$$D(\psi, \tilde{\psi}') = \sqrt{1 - |\langle \tilde{\psi}' | \psi \rangle|^2}, \quad (16)$$

where $|\tilde{\psi}'\rangle$ is the reconstructed state from $|\psi'\rangle$, and $|\psi\rangle$ is the true state (see Eq. 3.) The reconstructed state is calculated from Eq. (7) and Eq. (10) for C1 and C2, respectively, which provides information about the true quantum state from the measurement results. By averaging $D(\psi, \tilde{\psi}')$ over many repetitions of the measurement procedure, we obtain the mean trace distance $\overline{D}(\psi, \tilde{\psi}')$, which yields slightly different of the true state [1].

First, we numerically examine the mean trace distance $\overline{D}(\psi, \tilde{\psi}')$ versus the number of copies N . The results are shown in Fig. 2 for several well-known quantum

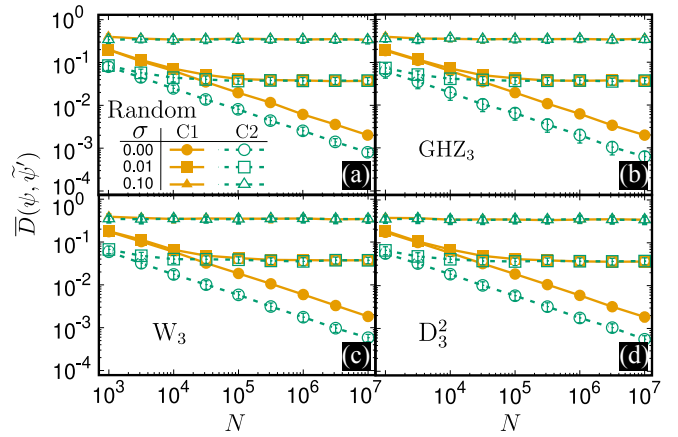


FIG. 2. Log-log plot of the mean trace distance $\overline{D}(\psi, \tilde{\psi}')$ as a function of the number of copies N for various standard states: (a) random state, (b) Greenberger-Horne-Zeilinger GHZ_3 state, (c) W_3 state, (d) D_3^2 state. For each case, the results from C1 (filled symbols) and C2 (open symbols) are plotted for several errors: $\sigma = 0.00, 0.01, 0.10$ and 0.10.

states: (a) random state (distributed following Haar measure [37]), (b) Greenberger-Horne-Zeilinger GHZ_3 state, i.e., $\text{GHZ}_3 = 1/\sqrt{2}(|000\rangle + |111\rangle)$, (c) W_3 state, i.e., $\text{W}_3 = 1/\sqrt{3}(|001\rangle + |010\rangle + |100\rangle)$, and (d) Dicke state D_3^2 , i.e., $\text{D}_3^2 = 1/\sqrt{3}(|011\rangle + |101\rangle + |110\rangle)$. For each state, we consider several noisy parameters $\sigma = 0.00, 0.01, 0.10$ as examples. For simplicity, we choose the same noise parameter (σ) for the state preparation and state postselection.

For all cases without noise ($\sigma = 0.0$), $\overline{D}(\psi, \tilde{\psi}')$ continuously decreases as N increases, and C2 shows better results than C1. This observation can be understood as a consequence of the scan-free process in C2, where all postselected states $\{|n\rangle\}$ are kept for the reconstruction. This is a kind of “systematic error”, which typically depends on the different configurations of the measurement scheme [26]. The systematic error cannot be eliminated even though increasing the number of copies N (to eliminate the statistical error) as can be seen from the figure.

In the presence of noise, the state we measure $|\psi'\rangle$, is different from the initial state $|\psi\rangle$. Therefore, as a consequence, $\overline{D}(\psi, \tilde{\psi}')$ will first decrease and then quickly comes to saturate when increasing N . Furthermore, as can be seen from the figure, $\overline{D}(\psi, \tilde{\psi}')$ in C2 have a larger differential (the difference between with and without noise) in comparison to C1 case. This remark implies that C2 is more fragile against the noise than C1 because, in C2, the state-postselection noise is presented in the interaction ($|\mathbf{c}'_0\rangle$ in Eq. (8)) while in C1, this noise is mostly discarded through the postselection process. Interestingly, under the presence of noise, the systematic error is broken: there are no different in the measurement accuracies for the two configurations.

To further investigate the effect of noise, we examine $\overline{D}(\psi, \tilde{\psi}')$ as a function of the noise parameter σ . Here, we

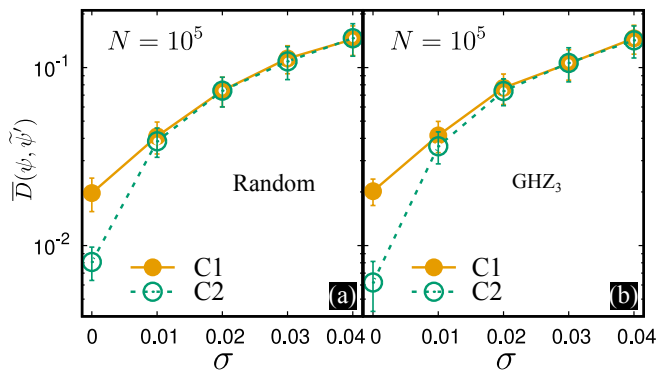


FIG. 3. Mean trace distance $\overline{D}(\psi, \tilde{\psi}')$ as a function of the noise parameter σ for two cases: (a) random state, (b) GHZ₃ state. For each case, two configurations C1 (filled circle) and C2 (open circle) are shown. The number of copies N is fixed at 10^5 which is believed large enough.

consider the random and GHZ₃ cases as they are well established, for example, see [38, 39]. These other cases can be analyzed similarly. The results are shown in Fig. 3 for a fixed $N = 10^5$. Obviously, in the absence of noise, the result from C2 is better than that one from C1. Whenever the noise increases, $\overline{D}(\psi, \tilde{\psi}')$ from C2 quickly increases and coincides with that one from C1 as an effect of the noise sensitivity as we discussed above. As a result, the systematic error is broken out when increasing the noise parameter σ .

B. Numerical results for mixed states

For the mixed-state case, we consider the GHZ state is transformed under the white noise such that $\rho'_0 = (1 - \epsilon)|\text{GHZ}_3\rangle\langle\text{GHZ}_3| + \epsilon\mathbf{I}_s/8$, where $0 \leq \epsilon \leq 1$ is the noise parameter. Such white noise transforms the state from the original (without noise) $\epsilon = 0$ to the maximum noise $\epsilon = 1$. The trace distance is defined by

$$D(\rho_0, \tilde{\rho}) = \frac{1}{2} \text{Tr} |\tilde{\rho} - \rho_0|. \quad (17)$$

In Fig. 4, we examine the mean trace distance $\overline{D}(\rho_0, \tilde{\rho})$ over the noisy state-preparation parameter ϵ and the noisy state-postselection parameter σ . In general, $\overline{D}(\rho_0, \tilde{\rho})$ increases when increasing ϵ and σ . Notably, when the state-preparation reaches the maximum noise $\epsilon = 1$, then $\overline{D}(\rho_0, \tilde{\rho})$ also reaches the maximum regardless the noisy state-postselection σ . Obviously, the noisy state-preparation plays a decisive role in the accuracy of the tomography process.

To look more detailed the accuracy in the two configurations C1 and C2, we extracted out some values from Fig. 4 and plot them in Fig. 5(a). First, let us consider the noiseless case, i.e., $\epsilon = 0$ and $\sigma = 0$, as indicated by the arrows in Fig. 5(a). In this case, $\overline{D}(\rho_0, \tilde{\rho})$ for C1 is better than C2. Again, this is the systematic error caused by different configurations.

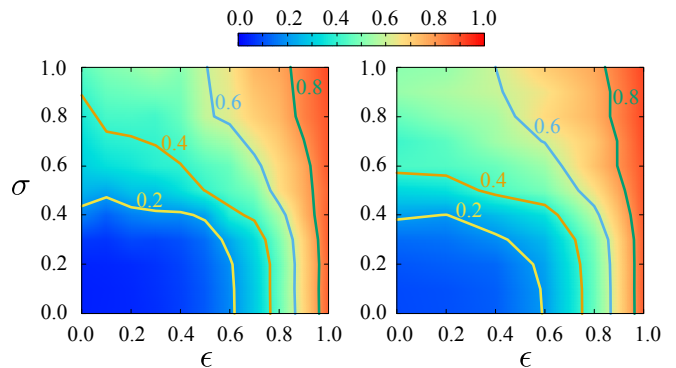


FIG. 4. Density plot of the mean trace distance $\overline{D}(\rho_0, \tilde{\rho})$ as a function of ϵ and σ for $N = 10^3$. Two configurations C1 (left) and C2 (right) are plotted and compared.

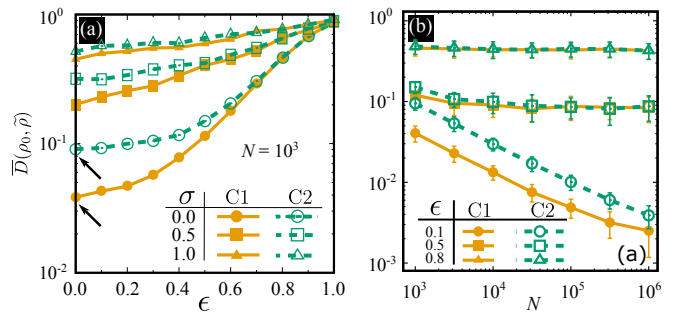


FIG. 5. (a) Plot of $\overline{D}(\rho_0, \tilde{\rho})$ versus ϵ for several σ 's as shown in the figure. The results are extracted from Fig. 4. Two configurations C1 and C2 are plotted and compared. The arrows indicate the case $\epsilon = \sigma = 0$. (b) Log-log plot of $\overline{D}(\rho_0, \tilde{\rho})$ as a function of N for $\epsilon = 0.1, 0.05, \text{ and } 0.8$ at fixed $\sigma = 0.05$.

When the noises are presented ($\epsilon \neq 0$ and $\sigma \neq 0$), $\overline{D}(\rho_0, \tilde{\rho})$ in C1 quickly increases and reaches that increasing in C2. For $\epsilon \rightarrow 1$, all $\overline{D}(\rho_0, \tilde{\rho})$ s converge regardless σ as we have mentioned above. This observation implies that when the SPAM errors appear and large enough, the systematic error will be broken out. For supporting our argument, we plot $\overline{D}(\rho_0, \tilde{\rho})$ as a function of N in Fig. 5(b) for several ϵ 's at fixed $\sigma = 0.05$. It can be seen that $\overline{D}(\rho_0, \tilde{\rho})$ behaves similarly to the pure-state case, where it comes to saturate (and converge) for large N whenever the noise is presented. Obviously, when increasing N large enough to eliminate the statistical error, the systematic error will be broken out by noises, i.e., SPAM errors.

IV. PRECISION OF QUANTUM STATE TOMOGRAPHY UNDER NOISE

We analytically investigate the impact of the state-preparation error on the precision of quantum state tomography by using the features of quantum Fisher information. Typically, the estimation of a parameter θ

through an estimator will result in another value ($\tilde{\theta}$) which is, in general, different from θ . The variance between θ and $\tilde{\theta}$ is then given by $\Delta^2\theta = \mathbb{E}(\tilde{\theta}^2) - \mathbb{E}^2(\tilde{\theta})$ (\mathbb{E} the average value,) and has a lower bound imposed by quantum mechanics:

$$\Delta^2\theta \geq \frac{1}{Q_\theta}, \quad (18)$$

is called quantum Cramér-Rao bound, where Q_θ is the quantum Fisher information (QFI) corresponding to the maximization over all possible measurements of the optimal estimator [1]. This is the ultimate achievable precision in the estimation of θ .

In our pure-state case, for a given quantum state without noise $|\psi\rangle = \sum_n \psi_n |n\rangle$. Without loss of generality, we can assume ψ_n is real because the real part and imaginary part of a wave function can be evaluated separately. From the quantum estimation theory, for each n , we evaluate the QFI by

$$Q_n = \langle \psi | \mathbf{L}^2 | \psi \rangle = 4[1 - |\psi_n|^2], \quad (19)$$

where $\mathbf{L} = 2(|\partial_{\psi_n}\psi\rangle\langle\psi| + |\psi\rangle\langle\partial_{\psi_n}\psi|)$ is the symmetric logarithmic derivative [40]. The total QFI is $Q = \sum_n Q_n = 4(d-1)$, which is the maximum information that the measurements can gain for the given state $|\psi\rangle$.

Similarly, for a quantum state contains some noises given by $|\psi'\rangle = \frac{1}{\mathcal{N}} \sum_n (\psi_n + \delta_n) |n\rangle$ as in Eq. (3), the total QFI is (see App. D)

$$Q' = \frac{4}{\mathcal{N}^2} (d-1), \quad (20)$$

where \mathcal{N} is the normalization constant. In the absence of noise, $\mathcal{N} = 1$ and thus, $Q' = Q$.

To evaluate the efficiency of the measurement, we can define the variances $\Delta^2\psi \propto Q^{-1}$ and $\Delta^2\psi' \propto [Q']^{-1}$ for cases of without and with noise, respectively. In Fig. 6, we examine the variances versus \mathcal{N} for $d = 8$. It can be seen that $\Delta^2\psi = 1/28$ is a constant, while $\Delta^2\psi' < \Delta^2\psi$ for $\mathcal{N} < 1$ and $\Delta^2\psi' \geq \Delta^2\psi$ for $\mathcal{N} \geq 1$. In other words, the state-preparation error can gain more information for $\mathcal{N} < 1$ while it loses information for $\mathcal{N} > 1$.

Furthermore, for a normal distribution of δ_n in $|\psi'\rangle$, the normalization constant \mathcal{N} obeys the normal distribution as we illustrate by the cyan curve in Fig. 6 for a random state $d = 8$. Suppose we compare these results for two cases of $\mathcal{N} < 1$ and $\mathcal{N} > 1$ under the statistical distribution of \mathcal{N} (highlighted areas), it always shows $\Delta^2\psi' \geq \Delta^2\psi$. The highlighted areas are given by the integral under the curves $\Delta^2\psi$ and $\Delta^2\psi'$ and bounded by a certain range of non-zero \mathcal{N} , i.e., $\mathcal{N} \in [0.5, 2.0]$, as can be seen from the figure. This result implies that the variance with noise is larger than that one without noise. When increasing the noise parameter σ , the distribution of \mathcal{N} shifts toward the right, which results in the increasing of $\Delta^2\psi'$ in the right highlighted area and decreasing in the left highlighted area, and thus losing precision.

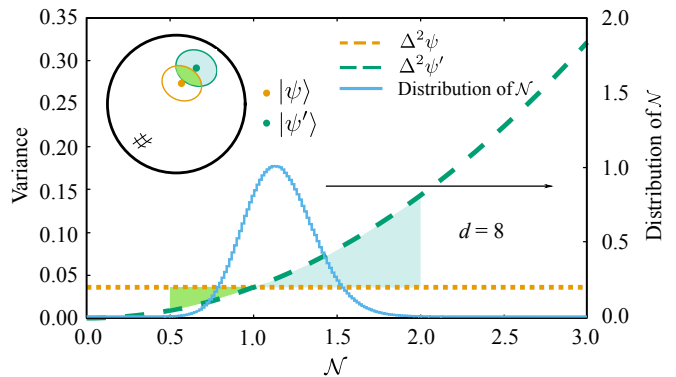


FIG. 6. The variances Δ^2 for two cases of without noise ($\Delta^2\psi$) and with noise ($\Delta^2\psi'$) as functions of the normalization constant \mathcal{N} . Here, \mathcal{N} obeys the normal distribution as numerically shown by the cyan normalized histogram (bottom-right axes.) The histogram was obtained from a random state for $d = 8$. Highlighted areas represent the differential between $\Delta^2\psi$ and $\Delta^2\psi'$ curves and can be calculated by taking the integral under these curves bounded by a certain range of non-zero \mathcal{N} . Inset: an illustration of distribution regions for the true state and the state-preparation error. Ideally, the reconstructed states will locate around the measured state, which forms a so-call distribution region. The orange dot and its rounded circle are the measured state and the distribution region when the measured state is the true state $|\psi\rangle$, likewise for the state-preparation error ($|\psi'\rangle$) indicated by the green dot and the distribution region is the green circle.

In the inset figure, we illustrate the distribution regions for these two cases of $|\psi\rangle$ and $|\psi'\rangle$. Here, the orange dot is the true state $|\psi\rangle$, and the orange circle is the distribution region where a reconstructed states $|\tilde{\psi}\rangle$ are located, likewise for the green dot indicates the noisy state $|\psi'\rangle$ and the distribution region of the reconstructed states $|\tilde{\psi}'\rangle$ is the green circle. There are situations (indicated by the lime area) that a reconstructed state $|\tilde{\psi}'\rangle$ is better than $|\tilde{\psi}\rangle$. These cases link to $\mathcal{N} < 1$ in the main figure. Inversely, the cyan area indicates those situations that $|\tilde{\psi}'\rangle$ is worse than $|\tilde{\psi}\rangle$, which connects to $\mathcal{N} > 1$ in the main figure. The illustration of these distribution regions thus directly leads to two different cases for \mathcal{N} , as can be seen from the main figure.

Overall, the state-preparation error gives less precision whenever the noise is presented regardless of how good measurement equipment is. We expect that appropriate optimal techniques, including quantum error correction and neural network architectures, could eliminate the SPAM errors [32, 41, 42].

V. CONCLUSION

We have numerically and analytically investigated the efficiency of the direct quantum state measurement (DSM) under the state-preparation-and-measurement (SPAM) errors by using quantum-controlled measure-

ments. We found that when the noisy state-preparation is presented, the measurement scheme gives less precise due to the bias between the true state and the state to be measured (the state that contains the noise.) Nevertheless, the noisy state-postselection has a significant effect on the measurement configurations, especially when combining with scan-free techniques in the DSM. Furthermore, under such a SPAM error, the systematic error will be broken, which results in the same accuracy for both configurations. Our study could provide an urgent outcome for understanding the effect of SPAM errors on quantum state tomography (QST). In comparison to the conventional QST, the DSM is more reliable in some particular cases such as high-dimension systems [14, 16, 43] and nonlocal entangled tomography [22]. However, a detailed comparison of the DSM efficiency and the conventional QST under noise requires much more investigation on quantum estimation theory. Thus, we leave it to the subject of future work. Further studies in this field also include error correction schemes and neural network architectures to eliminate SPAM errors.

ACKNOWLEDGMENTS

We would like to thank the anonymous referees for their valuable comments and suggestions. This work was supported by JSPS KAKENHI Grant Number 20F20021 and the Vietnam National University under Grant Number QG.20.17. LBH would like to thank Shikano for pointing out Ref. [30].

Appendix A: An example of noisy quantum state preparation

We provide an example for preparing the quantum state GHZ_3 that contains noise. Consider a quantum circuit as shown in Fig. 7 (inset). Therein, three qubits $q_0, q_1,$ and q_2 are prepared in the ground state, i.e., $|000\rangle$. Applying a sequence of Hadamard (H) gate onto q_0 , control-NOT ($CNOT$) gate onto $q_0, q_1,$ and control-NOT gate onto $q_0, q_2,$ as shown in the inset figure, respectively, we obtain the output state as

$$|000\rangle \xrightarrow{H} \frac{1}{\sqrt{2}}(|000\rangle + |100\rangle) \xrightarrow{CNOT} \frac{1}{\sqrt{2}}(|000\rangle + |110\rangle) \xrightarrow{CNOT} \frac{1}{\sqrt{2}}(|000\rangle + |111\rangle), \quad (\text{A.1})$$

which is the GHZ_3 state. We simulate this state in Fig. 7 (left) by using the IBM Qiskit package. It can be seen that the amplitudes of $|000\rangle$ and $|111\rangle$ are the same and equal to $1/\sqrt{2}$.

Now, let us assume the imperfection in the Hadamard gate as follows. We first decompose the Hadamard gate into the two rotations: $\pi/2$ about the Y-axis, and π about

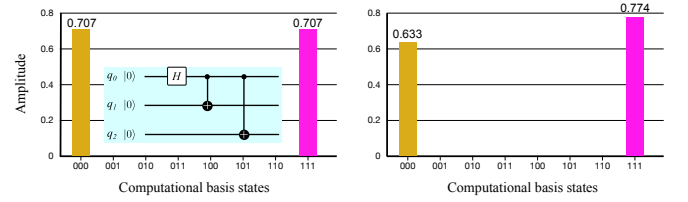


FIG. 7. Inset: Quantum circuit for generating GHZ_3 state. Initially, three qubits $q_0, q_1,$ and q_2 are prepared in the ground state, i.e., $|000\rangle$. Quantum Hadamard gate and Control-NOT gates are applied to transform the initial state to the desired state. See detailed in Appendix A. Left: the amplitudes of the components in the GHZ_3 state after applying H and $CNOT$ gates onto the initial state $|000\rangle$. Right: the amplitudes of the components in the GHZ_3 state under the imperfection of the Hadamard gate. These amplitudes are lightly deviated from the true values in the left figure.

the Z-axis, such that

$$-iH = \begin{pmatrix} \cos(\pi/4) & -\sin(\pi/4) \\ \sin(\pi/4) & \cos(\pi/4) \end{pmatrix} \begin{pmatrix} e^{-i\pi/2} & 0 \\ 0 & e^{i\pi/2} \end{pmatrix}, \quad (\text{A.2})$$

where the rotation matrices are given as

$$R_y(\theta) = \begin{pmatrix} \cos(\theta/2) & -\sin(\theta/2) \\ \sin(\theta/2) & \cos(\theta/2) \end{pmatrix}, \quad (\text{A.3})$$

$$R_z(\theta) = \begin{pmatrix} e^{-i\theta/2} & 0 \\ 0 & e^{i\theta/2} \end{pmatrix}. \quad (\text{A.4})$$

Under the imperfection, assume that the rotation angles will deviate from their true values, such as $\pi/2 + \alpha$, and $\pi + \beta$, where α and β are small angles. Without loss of generality, we can choose $\beta = 0$ since the operation of $R_z(\theta)$ does not affect the amplitudes of the quantum state. As a result, the Hadamard gate becomes

$$-iH' = \frac{1}{\sqrt{2}} \begin{pmatrix} \cos(\frac{\alpha}{2}) - \sin(\frac{\alpha}{2}) & \cos(\frac{\alpha}{2}) + \sin(\frac{\alpha}{2}) \\ \cos(\frac{\alpha}{2}) + \sin(\frac{\alpha}{2}) & -[\cos(\frac{\alpha}{2}) - \sin(\frac{\alpha}{2})] \end{pmatrix} = \frac{1}{\sqrt{2}} \begin{pmatrix} a & b \\ b & -a \end{pmatrix}. \quad (\text{A.5})$$

Therefore, the final state becomes

$$\frac{1}{\sqrt{2}}(a|000\rangle + b|111\rangle), \quad (\text{A.6})$$

which slightly different from the true GHZ_3 state. Here, $\frac{1}{2}(|a|^2 + |b|^2) = 1$. This is an example of a noisy state-preparation process. In Fig. 7 (right), we simulate the GHZ_3 state assuming that the Hadamard gate is under the imperfection at $\alpha = 0.2$ as an example. Under this noisy state-preparation, the two components $|000\rangle$ and $|111\rangle$ are deviated from $1/\sqrt{2}$. In general, all the components will be deviated from their values as we have modeled from Eq. 3 in the main text.

Appendix B: Quantum controlled measurements for pure states

In this appendix, we closely follow the quantum controlled measurement framework introduced by Ogawa et al. [29] for pure states, and we derive it under the noise using our denotation to make the work self-consistency.

We consider the initial joint state of the target system and the control qubit probe as $|\Psi\rangle = |\psi'\rangle \otimes |\xi\rangle$, where

$$|\psi'\rangle = \frac{1}{\mathcal{N}} \sum_{n=0}^{d-1} (\psi_n + \delta_n) |n\rangle = \sum_{n=0}^{d-1} \psi'_n |n\rangle, \quad \text{and} \quad (\text{B.1})$$

$$|\xi\rangle \equiv |+\rangle = \frac{1}{\sqrt{2}} (|0\rangle + |1\rangle), \quad (\text{B.2})$$

where \mathcal{N} is the normalization factor, $\psi'_n = \frac{\psi_n + \delta_n}{\mathcal{N}}$, and $\delta_n = x_1 + ix_2$ is a complex random number, where x_1 and x_2 are random numbers that follow the normal distribution $f(x) = \frac{1}{\sigma\sqrt{2\pi}} \exp[-\frac{1}{2}(\frac{x}{\sigma})^2]$.

For C1

For C1, following Ogawa et al. [29], we consider the interaction as

$$\mathbf{U}_n = (\mathbf{I}_s - |n\rangle\langle n|) \otimes |0\rangle\langle 0| + |n\rangle\langle n| \otimes |1\rangle\langle 1|. \quad (\text{B.3})$$

After the interaction, the joint state becomes

$$\mathbf{U}_n |\Psi\rangle = \frac{1}{\sqrt{2}} \left[\sum_{m=0}^{d-1} \psi'_m |m\rangle - \psi'_n |n\rangle \right] \otimes |0\rangle + \frac{1}{\sqrt{2}} \psi'_n |n\rangle \otimes |1\rangle. \quad (\text{B.4})$$

We postselect the target system onto the conjugate basis

$$|\zeta'_0\rangle = \frac{1}{\mathcal{M}} \sum_{m=0}^{d-1} (1 + \kappa_m) |m\rangle = \sum_{m=0}^{d-1} \mathbf{c}_m |m\rangle, \quad (\text{B.5})$$

where \mathcal{M} is the normalization factor, and $\mathbf{c}_m = \frac{1 + \kappa_m}{\mathcal{M}}$. Here, κ_m is a real random number and distributes according to the normal distribution. The final control qubit state is given by

$$\begin{aligned} |\eta\rangle &= (\langle \zeta'_0 | \otimes \mathbf{I}_p) \mathbf{U}_n |\Psi\rangle \\ &= \frac{1}{\sqrt{2}} \left[(\Gamma - \mathbf{c}_n \psi'_n) |0\rangle + \mathbf{c}_n \psi'_n |1\rangle \right], \end{aligned} \quad (\text{B.6})$$

where $\Gamma = \sum_{m=0}^{d-1} \mathbf{c}_m \psi'_m$.

Finally, we measure the control qubit probe in the Pauli basis $|j\rangle \in \{|0\rangle, |1\rangle, |+\rangle, |-\rangle, |L\rangle, |R\rangle\}$, where $|\pm\rangle = \frac{1}{\sqrt{2}} (|0\rangle \pm |1\rangle)$, $|L\rangle = \frac{1}{\sqrt{2}} (|0\rangle + i|1\rangle)$, $|R\rangle = \frac{1}{\sqrt{2}} (|0\rangle - i|1\rangle)$. The probability for measuring $|j\rangle\langle j|$ is $P_j = |\langle j|\eta\rangle|^2$ ex-

plicitly give

$$P_0 = \frac{1}{2} \left[\Gamma^2 - 2\mathbf{c}_n \Gamma \text{Re}\psi'_n + \mathbf{c}_n^2 |\psi'_n|^2 \right], \quad (\text{B.7})$$

$$P_1 = \frac{1}{2} \mathbf{c}_n^2 |\psi'_n|^2, \quad (\text{B.8})$$

$$P_+ = \frac{1}{4} \Gamma^2, \quad (\text{B.9})$$

$$P_- = \frac{1}{4} \left[\Gamma^2 - 4\Gamma \mathbf{c}_n \text{Re}\psi'_n + 4\mathbf{c}_n^2 |\psi'_n|^2 \right], \quad (\text{B.10})$$

$$P_L = \frac{1}{4} \left[\Gamma^2 - 2\Gamma \mathbf{c}_n \text{Re}\psi'_n + 2\Gamma \mathbf{c}_n \text{Im}\psi'_n + 2\mathbf{c}_n^2 |\psi'_n|^2 \right], \quad (\text{B.11})$$

$$P_R = \frac{1}{4} \left[\Gamma^2 - 2\Gamma \mathbf{c}_n \text{Re}\psi'_n - 2\Gamma \mathbf{c}_n \text{Im}\psi'_n + 2\mathbf{c}_n^2 |\psi'_n|^2 \right]. \quad (\text{B.12})$$

As a result, the real and imaginary parts of the amplitude ψ'_n are reproduced as

$$\text{Re}\psi'_n = \frac{P_+ - P_- + 2P_1}{\mathbf{c}_n \Gamma}, \quad \text{Im}\psi'_n = \frac{P_L - P_R}{\mathbf{c}_n \Gamma}. \quad (\text{B.13})$$

For C2

For C2, the interaction is given by [29]

$$\mathbf{U} = (\mathbf{I}_s - |\zeta'_0\rangle\langle \zeta'_0|) \otimes |0\rangle\langle 0| + |\zeta'_0\rangle\langle \zeta'_0| \otimes |1\rangle\langle 1|. \quad (\text{B.14})$$

The joint state after the interaction is given by

$$\begin{aligned} \mathbf{U} |\Psi\rangle &= \frac{1}{\sqrt{2}} \left[\sum_{m=0}^{d-1} \psi'_m |m\rangle - \sum_{m=0}^{d-1} \psi'_m \mathbf{c}_m |\zeta'_0\rangle \right] \otimes |0\rangle \\ &+ \frac{1}{\sqrt{2}} \left[\sum_{m=0}^{d-1} \psi'_m \mathbf{c}_m |\zeta'_0\rangle \right] \otimes |1\rangle. \end{aligned} \quad (\text{B.15})$$

After the interaction, the target system is postselected onto $|n\rangle$ while the remaining state of the control qubit probe is given as

$$|\eta\rangle = \frac{1}{\sqrt{2}} \left[(\psi'_n - \mathbf{c}_n \Gamma) |0\rangle + \mathbf{c}_n \Gamma |1\rangle \right]. \quad (\text{B.16})$$

Measuring the control qubit probe in the Pauli basis as above, we obtain

$$P_0 = \frac{1}{2} \left[|\psi'_n|^2 - 2\mathbf{c}_n \Gamma \text{Re}\psi'_n + \mathbf{c}_n^2 \Gamma^2 \right], \quad (\text{B.17})$$

$$P_1 = \frac{1}{2} \mathbf{c}_n^2 \Gamma^2, \quad (\text{B.18})$$

$$P_+ = \frac{1}{4} |\psi'_n|^2, \quad (\text{B.19})$$

$$P_- = \frac{1}{4} \left[|\psi'_n|^2 - 4\mathbf{c}_n \Gamma \text{Re}\psi'_n + 4\mathbf{c}_n^2 \Gamma^2 \right], \quad (\text{B.20})$$

$$P_L = \frac{1}{4} \left[|\psi'_n|^2 - 2\mathbf{c}_n \Gamma \text{Re}\psi'_n + 2\mathbf{c}_n \Gamma \text{Im}\psi'_n + 2\mathbf{c}_n^2 \Gamma^2 \right], \quad (\text{B.21})$$

$$P_R = \frac{1}{4} \left[|\psi'_n|^2 - 2\mathbf{c}_n \Gamma \text{Re}\psi'_n - 2\mathbf{c}_n \Gamma \text{Im}\psi'_n + 2\mathbf{c}_n^2 \Gamma^2 \right]. \quad (\text{B.22})$$

Then, we have

$$\text{Re}\psi'_n = \frac{P_+ - P_- + 2P_1}{\mathbf{c}_n\Gamma}, \quad \text{Im}\psi'_n = \frac{P_L - P_R}{\mathbf{c}_n\Gamma}. \quad (\text{B.23})$$

Appendix C: Quantum controlled measurements for mixed states

We consider the joint state Λ as following

$$\Lambda = \rho'_0 \otimes |+\rangle\langle+|, \quad \text{with } \rho'_0 = \sum_{n,m=0}^{d-1} \rho'_{nm} |n\rangle\langle m|. \quad (\text{C.1})$$

For C1

The interaction operator is given the same as above:

$$\mathbf{U}_n = (\mathbf{I}_s - |n\rangle\langle n|) \otimes |0\rangle\langle 0| + |n\rangle\langle n| \otimes |1\rangle\langle 1|. \quad (\text{C.2})$$

After the interaction, the joint state evolves to

$$\Lambda' = \mathbf{U}_n \Lambda \mathbf{U}_n^\dagger, \quad (\text{C.3})$$

which is explicitly written as

$$\begin{aligned} \Lambda' &= \left[\rho'_0 - \left(\sum_{m=0}^{d-1} \rho'_{nm} |n\rangle\langle m| + c.c \right) + \rho'_{nn} |n\rangle\langle n| \right] \otimes \frac{1}{2} |0\rangle\langle 0| \\ &+ \left[\sum_{m=0}^{d-1} \rho'_{mn} |m\rangle\langle n| - \rho'_{nn} |n\rangle\langle n| \right] \otimes \frac{1}{2} |0\rangle\langle 1| \\ &+ \left[\sum_{m=0}^{d-1} \rho'_{nm} |n\rangle\langle m| - \rho'_{nn} |n\rangle\langle n| \right] \otimes \frac{1}{2} |1\rangle\langle 0| \\ &+ \left[\rho'_{nn} |n\rangle\langle n| \right] \otimes \frac{1}{2} |1\rangle\langle 1|. \end{aligned} \quad (\text{C.4})$$

Here, *c.c* stands for ‘complex conjugate.’ After postselecting this state onto

$$\begin{aligned} |\mathbf{c}'_k\rangle\langle \mathbf{c}'_k| &= \frac{1}{\mathcal{M}^2} \sum_{n,m=0}^{d-1} e^{i2\pi(m-n)k/d} (1 + \kappa_m)(1 + \kappa_n) |m\rangle\langle n| \\ &= \sum_{n,m=0}^{d-1} e^{i2\pi(m-n)k/d} \mathbf{c}_m \mathbf{c}_n |m\rangle\langle n|, \end{aligned} \quad (\text{C.5})$$

the final state of the control qubit probe becomes

$$\Lambda'' = \langle \mathbf{c}'_k | \Lambda' | \mathbf{c}'_k \rangle = \begin{pmatrix} \Lambda''_{00}(n, k) & \Lambda''_{01}(n, k) \\ \Lambda''_{10}(n, k) & \Lambda''_{11}(n, k) \end{pmatrix}. \quad (\text{C.6})$$

Explicitly,

$$\begin{aligned} \Lambda''_{00}(n, k) &= \frac{1}{2} \left[\sum_{n,m=0}^{d-1} \rho'_{nm} e^{i2\pi(m-n)k/d} \mathbf{c}_m \mathbf{c}_n \right. \\ &\left. - \left(\sum_{m=0}^{d-1} \rho'_{nm} e^{i2\pi(m-n)k/d} \mathbf{c}_n \mathbf{c}_m + c.c \right) + \rho'_{nn} \mathbf{c}_n^2 \right] \end{aligned} \quad (\text{C.7})$$

$$\Lambda''_{01}(n, k) = \frac{1}{2} \left[\sum_{m=0}^{d-1} \rho'_{mn} e^{i2\pi(n-m)k/d} \mathbf{c}_n \mathbf{c}_m - \rho'_{nn} \mathbf{c}_n^2 \right] \quad (\text{C.8})$$

$$\Lambda''_{10}(n, k) = [\Lambda''_{01}(n, k)]^* \quad (\text{C.9})$$

$$\Lambda''_{11}(n, k) = \frac{1}{2} \rho'_{nn} \mathbf{c}_n^2. \quad (\text{C.10})$$

Using Fourier transformation on $\Lambda''_{10}(n, k)$, we obtain

$$\rho'_{nm} \propto \frac{1}{\mathbf{c}_n \mathbf{c}_m} \left[d \delta_{n,m} \Lambda''_{11}(n, k) + \sum_{k=0}^{d-1} e^{i2\pi(n-m)k/d} \Lambda''_{10}(n, k) \right]. \quad (\text{C.11})$$

To get $\Lambda''_{10}(n, k)$ and $\Lambda''_{11}(n, k)$, the control qubit is measured as follows:

$$\Lambda''_{10}(n, k) = \frac{1}{2} [(P_+ - P_-) + i(P_L - P_R)], \quad \text{and} \quad (\text{C.12})$$

$$\Lambda''_{11}(n, k) = P_1, \quad (\text{C.13})$$

where $P_j = \text{Tr}[|j\rangle\langle j| \Lambda'']$ is the probability when measuring the control qubit probe in the element j of the Pauli basis.

For C2

In this case, the interaction is

$$\mathbf{U} = (\mathbf{I}_s - |\mathbf{c}'_k\rangle\langle \mathbf{c}'_k|) \otimes |0\rangle\langle 0| + |\mathbf{c}'_k\rangle\langle \mathbf{c}'_k| \otimes |1\rangle\langle 1|. \quad (\text{C.14})$$

After applying this interaction \mathbf{U} , the initial joint state becomes

$$\Lambda' = \mathbf{U} \Lambda \mathbf{U}^\dagger, \quad (\text{C.15})$$

which is explicitly given as

$$\begin{aligned}
\Lambda' = & \left[\rho'_0 - \sum_{n,m=0}^{d-1} \rho'_{nm} \mathbf{c}_m e^{i2\pi km/d} |n\rangle \langle \mathbf{c}'_k| - |\mathbf{c}'_k\rangle \sum_{n,m=0}^{d-1} \rho'_{nm} \mathbf{c}_n e^{-i2\pi kn/d} \langle m| \right. \\
& \left. + \sum_{n,m=0}^{d-1} \rho'_{nm} \mathbf{c}_n \mathbf{c}_m e^{i2\pi k(m-n)/d} |\mathbf{c}'_k\rangle \langle \mathbf{c}'_k| \right] \otimes \frac{1}{2} |0\rangle \langle 0| \\
& + \left[\sum_{n,m=0}^{d-1} \rho'_{nm} \mathbf{c}_m e^{i2\pi km/d} |n\rangle \langle \mathbf{c}'_k| - \sum_{n,m=0}^{d-1} \rho'_{nm} \mathbf{c}_n \mathbf{c}_m e^{i2\pi k(m-n)/d} |\mathbf{c}'_k\rangle \langle \mathbf{c}'_k| \right] \otimes \frac{1}{2} |0\rangle \langle 1| \\
& + \left[|\mathbf{c}'_k\rangle \sum_{n,m=0}^{d-1} \rho'_{nm} \mathbf{c}_n e^{-i2\pi kn/d} \langle m| - \sum_{n,m=0}^{d-1} \rho'_{nm} \mathbf{c}_n \mathbf{c}_m e^{i2\pi k(m-n)/d} |\mathbf{c}'_k\rangle \langle \mathbf{c}'_k| \right] \otimes \frac{1}{2} |1\rangle \langle 0| \\
& + \left[\sum_{n,m=0}^{d-1} \rho'_{nm} \mathbf{c}_n \mathbf{c}_m e^{i2\pi k(m-n)/d} |\mathbf{c}'_k\rangle \langle \mathbf{c}'_k| \right] \otimes \frac{1}{2} |1\rangle \langle 1|. \tag{C.16}
\end{aligned}$$

Next, we postselect this state onto $|n\rangle \langle n|$ and get

$$\Lambda'' = \langle n | \Lambda' | n \rangle = \begin{pmatrix} \Lambda''_{00}(n, k) & \Lambda''_{01}(n, k) \\ \Lambda''_{10}(n, k) & \Lambda''_{11}(n, k) \end{pmatrix}. \tag{C.17}$$

Explicitly,

$$\begin{aligned}
\Lambda''_{00}(n, k) = & \frac{1}{2} \left[\rho'_{nn} - \left(\sum_{m=0}^{d-1} \rho'_{nm} \mathbf{c}_m \mathbf{c}_n e^{i2\pi k(m-n)/d} + c.c. \right) \right. \\
& \left. + \left(\sum_{n,m=0}^{d-1} \rho'_{nm} \mathbf{c}_n \mathbf{c}_m e^{i2\pi k(m-n)/d} \right) \mathbf{c}_n^2 \right], \tag{C.18}
\end{aligned}$$

$$\begin{aligned}
\Lambda''_{01}(n, k) = & \frac{1}{2} \left[\left(\sum_{m=0}^{d-1} \rho'_{nm} \mathbf{c}_m \mathbf{c}_n e^{i2\pi k(m-n)/d} \right) \right. \\
& \left. - \left(\sum_{n,m=0}^{d-1} \rho'_{nm} \mathbf{c}_n \mathbf{c}_m e^{i2\pi k(m-n)/d} \right) \mathbf{c}_n^2 \right], \tag{C.19}
\end{aligned}$$

$$\Lambda''_{10}(n, k) = [\Lambda''_{01}(n, k)]^*, \tag{C.20}$$

$$\Lambda''_{11}(n, k) = \frac{1}{2} \left[\sum_{n,m=0}^{d-1} \rho'_{nm} \mathbf{c}_n \mathbf{c}_m e^{i2\pi k(m-n)/d} \right] \mathbf{c}_n^2. \tag{C.21}$$

Using Fourier transformation on $\Lambda''_{01}(n, k)$, we obtain:

$$\rho'_{nm} \propto \frac{1}{\mathbf{c}_m \mathbf{c}_n} \left[\sum_{k=0}^{d-1} e^{i2\pi k(n-m)/d} \left(\Lambda''_{01}(n, k) + \Lambda''_{11}(n, k) \right) \right], \tag{C.22}$$

where $\Lambda''_{01}(n, k)$ is obtained by measuring the control qubit probe as follows:

$$\Lambda''_{01}(n, k) = \frac{1}{2} \left[(P_+ - P_-) - i(P_L - P_R) \right]. \tag{C.23}$$

Appendix D: Quantum Fisher Information

In this section, we show how to calculate the total quantum Fisher information (QFI) for $|\psi'\rangle$ state:

$$|\psi'\rangle = \frac{1}{\mathcal{N}} \sum_{n=0}^{d-1} (\psi_n + \delta_n) |n\rangle, \tag{D.1}$$

where ψ_n is unknown. The normalization constant is

$$\mathcal{N}^2 = \sum_{n=0}^{d-1} (\psi_n + \delta_n)^2. \tag{D.2}$$

Here, note that we consider both ψ_n and δ_n are real for simplicity. First, we calculate $\partial_{\psi_n} |\psi'\rangle$, where we are using ∂_{ψ_n} as shorthand for $\partial/\partial\psi_n$. We have

$$\begin{aligned}
\partial_{\psi_n} |\psi'\rangle = & \frac{\partial}{\partial\psi_n} \left(\frac{1}{\mathcal{N}} \sum_{n=0}^{d-1} (\psi_n + \delta_n) |n\rangle \right) \\
& + \frac{1}{\mathcal{N}} \frac{\partial}{\partial\psi_n} \left(\sum_{n=0}^{d-1} (\psi_n + \delta_n) |n\rangle \right) \\
= & -\frac{\psi_n + \delta_n}{\mathcal{N}^2} |\psi'\rangle + \frac{1}{\mathcal{N}} |n\rangle. \tag{D.3}
\end{aligned}$$

The Quantum Fisher Information (QFI) is given by

$$\begin{aligned}
Q'_n = & 4 \left[\frac{\langle \partial\psi' | \partial\psi' \rangle}{\partial\psi_n \partial\psi_n} - \left| \frac{\langle \partial\psi' | \psi' \rangle}{\partial\psi_n} \right|^2 \right], \\
= & \frac{4}{\mathcal{N}^2} \left[1 - \frac{(\psi_n + \delta_n)^2}{\mathcal{N}^2} \right]. \tag{D.4}
\end{aligned}$$

Then, the total QFI is

$$Q' = \sum_{n=0}^{d-1} Q'_n = \frac{4}{\mathcal{N}^2} (d-1). \tag{D.5}$$

-
- [1] M. Paris and J. Řeháček (Eds), *Quantum State Estimation*, Lecture Notes in Physics, Vol. 649 (Springer-Verlag, Berlin Heidelberg, 2004).
- [2] J. Helsen, X. Xue, L. M. K. Vandersypen, and S. Wehner, npj Quantum Information **5**, 71 (2019).
- [3] F. Frank, T. Uden, J. Zoller, R. S. Said, T. Calarco, S. Montangero, B. Naydenov, and F. Jelezko, npj Quantum Information **3**, 48 (2017).
- [4] A. Gheorghiu, T. Kapourniotis, and E. Kashefi, Theory of Computing Systems **63**, 715 (2019).
- [5] J. Preskill, Quantum **2**, 79 (2018).
- [6] M. Schlosshauer, *Decoherence and the quantum-to-classical transition* (Springer, 2007).
- [7] C. Jackson and S. J. van Enk, Phys. Rev. A **92**, 042312 (2015).
- [8] H. Kosaka, T. Inagaki, Y. Rikitake, H. Imamura, Y. Mitsumori, and K. Edamatsu, Nature **457**, 702 (2009).
- [9] M. R. Vanner, J. Hofer, G. D. Cole, and M. Aspelmeyer, Nature Communications **4**, 2295 (2013).
- [10] D. Lu, T. Xin, N. Yu, Z. Ji, J. Chen, G. Long, J. Baugh, X. Peng, B. Zeng, and R. Laflamme, Phys. Rev. Lett. **116**, 230501 (2016).
- [11] C. H. Baldwin, I. H. Deutsch, and A. Kalev, Phys. Rev. A **93**, 052105 (2016).
- [12] J. S. Lundeen, B. Sutherland, A. Patel, C. Stewart, and C. Bamber, Nature **474**, 188 (2011).
- [13] J. S. Lundeen and C. Bamber, Phys. Rev. Lett. **108**, 070402 (2012).
- [14] Z. Shi, M. Mirhosseini, J. Margiewicz, M. Malik, F. Rivera, Z. Zhu, and R. W. Boyd, Optica **2**, 388 (2015).
- [15] M. Mirhosseini, O. S. Magaña Loaiza, S. M. Hashemi Rafsanjani, and R. W. Boyd, Phys. Rev. Lett. **113**, 090402 (2014).
- [16] M. Malik, M. Mirhosseini, M. P. J. Lavery, J. Leach, M. J. Padgett, and R. W. Boyd, Nature Communications **5**, 3115 (2014).
- [17] E. Bolduc, G. Gariépy, and J. Leach, Nature Communications **7**, 10439 (2016).
- [18] S. H. Knarr, D. J. Lum, J. Schneeloch, and J. C. Howell, Phys. Rev. A **98**, 023854 (2018).
- [19] G. S. Thekkadath, L. Giner, Y. Chalich, M. J. Horton, J. Banker, and J. S. Lundeen, Phys. Rev. Lett. **117**, 120401 (2016).
- [20] L. Calderaro, G. Foletto, D. Dequal, P. Villoresi, and G. Vallone, Phys. Rev. Lett. **121**, 230501 (2018).
- [21] L. B. Ho, Physics Letters A **383**, 289 (2019).
- [22] W.-W. Pan, X.-Y. Xu, Y. Kedem, Q.-Q. Wang, Z. Chen, M. Jan, K. Sun, J.-S. Xu, Y.-J. Han, C.-F. Li, and G.-C. Guo, Phys. Rev. Lett. **123**, 150402 (2019).
- [23] J. A. Gross, N. Dangniam, C. Ferrie, and C. M. Caves, Phys. Rev. A **92**, 062133 (2015).
- [24] I. Sainz and A. B. Klimov, EPL (Europhysics Lett.) **116**, 10002 (2016).
- [25] S. Pang, J. R. G. Alonso, T. A. Brun, and A. N. Jordan, Phys. Rev. A **94**, 012329 (2016).
- [26] L. B. Ho, Journal of Physics B: Atomic, Molecular and Optical Physics **47**, 124101 (2014).
- [27] J. von Neumann, *Mathematical Foundations of Quantum Mechanics: New Edition* (Princeton University Press, 2018).
- [28] H. F. Hofmann, New Journal of Physics **16**, 063056 (2014).
- [29] K. Ogawa, O. Yasuhiko, H. Kobayashi, T. Nakanishi, and A. Tomita, New Jour. of Phys. **21**, 043013 (2019).
- [30] Y. Shikano and A. Hosoya, Journal of Physics A: Mathematical and Theoretical **43**, 025304 (2010).
- [31] T. Weiss and O. Romero-Isart, Phys. Rev. Research **1**, 033157 (2019).
- [32] A. M. Palmieri, E. Kovlakov, F. Bianchi, D. Yudin, S. Straupe, J. D. Biamonte, and S. Kulik, npj Quantum Information **6**, 20 (2020).
- [33] G. Vallone and D. Dequal, Phys. Rev. Lett. **116**, 040502 (2016).
- [34] M. A. Nielsen and I. L. Chuang, *Quantum computation and quantum information* (Cambridge University Press, 2000).
- [35] L. Maccone and C. C. Rusconi, Phys. Rev. A **89**, 022122 (2014).
- [36] L. B. Ho, K. Q. Tuan, and H. Q. Nguyen, Computer Physics Communications **263**, 107902 (2021).
- [37] F. Mezzadri, Notices of the American Mathematical Society **54**, 592 (2007).
- [38] G. Carvacho, F. Graffitti, V. D'Ambrosio, B. C. Hiesmayr, and F. Sciarrino, Scientific Reports **7**, 13265 (2017).
- [39] D.-X. Li, T.-Y. Zheng, and X.-Q. Shao, Opt. Express **27**, 20874 (2019).
- [40] M. G. A. PARIS, International Journal of Quantum Information **07**, <https://doi.org/10.1142/S0219749909004839>.
- [41] M. A. Nielsen, C. M. Caves, B. Schumacher, and H. Barnum, Proceedings of the Royal Society of London. Series A: Mathematical and Physical Sciences **464**, 2571 (2000).
- [42] Y. Watanabe, T. Sagawa, and M. Ueda, Phys. Rev. Lett. **104**, 020401 (2010).
- [43] M. Yang, Y. Xiao, Y.-W. Liao, Z.-H. Liu, X.-Y. Xu, J.-S. Xu, C.-F. Li, and G.-C. Guo, Laser & Photonics Reviews **14**, 1900251 (2020).